IEEE Access
Multidisciplinary ⋮ Rapid Review ⋮ Open Access Journal

Received 15 December 2022, accepted 1 February 2023, date of publication 3 February 2023, date of current version 8 February 2023.

Digital Object Identifier 10.1109/ACCESS.2023.3242602

RESEARCH ARTICLE

A Novel Design for Dual-Band Wearable Textile Eighth-Mode SIW Antennas

GIOVANNI ANDREA CASULA, (Senior Member, IEEE), GIORGIO MONTISCI, (Senior Member, IEEE), AND GIACOMO MUNTONI

Dipartimento di Ingegneria Elettrica ed Elettronica, Università degli Studi di Cagliari, 09123 Cagliari, Italy

Corresponding author: Giorgio Montisci (giorgio.montisci@unica.it)

ABSTRACT A novel wearable textile dual-band antenna configuration based on a substrate integrated waveguide (SIW) cavity is presented. The miniaturization of the antenna is achieved by exploiting the magnetic field symmetry of a square SIW cavity, reducing its size to 1/8 of the full square cavity with an eighth-mode SIW configuration. This solution is applied to the design of a wearable dual-band antenna for Long Range (LoRa) applications. The antenna operating frequency covers both the UHF LoRa bands, the European (863-870 MHz) and the North American (902-928 MHz). The proposed design provides a low-cost and compact antenna, which is easy to fabricate and ensures a very good isolation and robustness with respect to the human body proximity. The commercial software CST Studio Suite has been used for the antenna design and simulations. A prototype has been fabricated and the measured results are in good agreement with numerical simulations.

INDEX TERMS Body-antenna coupling, eighth-mode substrate integrated waveguide (EMSIW), substrate integrated waveguide (SIW), textile antennas, wearable antennas.

I. INTRODUCTION

In recent years, the evolution of miniaturization techniques for wireless devices and for smart networks and systems design resulted in a prompt diffusion of body area networks and personal area networks. These new generation networks play a pivotal role in many different fields, such as personal healthcare, smart home, sport, military, space, entertainment. In the near future, we are likely to carry and wear several devices and sensors simultaneously, that will constantly communicate with each other and with the outside world. These functionalities should be provided as unobtrusively and comfortable as possible to facilitate their usage. Thankfully, the technology behind wearable electronics and antennas has undergone a considerable advancement [1], [2].

Antennas for wearable applications should be easily and effectively integrated into a garment, and this requires an adequate mechanical robustness, and a fabrication process as simple as possible. These antennas must be comfortable for the wearer, compact, lightweight, robust enough with respect to the proximity with the human body, and low-cost. They are often constructed using conductive fabric [3], [4], [5] and are usually characterized by low gain and efficiency, since they work close, or attached, to the human body. In addition, wearable antennas are particularly sensitive to the deployment conditions and to their distance with respect to the wearer's body.

An antenna structure entirely made using flexible textiles can be both easily integrated into commercial cloths, and conformal to the human body. Hence, an important requirement is the antenna flexibility and bending, due to the unpredictable movements of the wearer, and this calls for an accurate evaluation on the effect of antenna deformation on its performance.

All wearable antennas have some unwanted backward radiation, which is absorbed by the human tissues. This radiation can be hazardous if it exceeds the standard exposure limit. Therefore, for on-body applications, the SAR guidelines for electromagnetic radiation absorption must be considered and fulfilled.

The associate editor coordinating the review of this manuscript and approving it for publication was Tutku Karacolak.

This work is licensed under a Creative Commons Attribution 4.0 License. For more information, see https://creativecommons.org/licenses/by/4.0/

TABLE 1. Comparison between the wearable dual-band SIW antennas proposed in the literature. The antenna size is normalized to the free-space wavelength λ_0 at the operating frequency.

Ref.	Operating frequency (GHz)	Normalized antenna size	Substrate (ε_r)	Bandwidth (%)	Peak gain (dBi)	Material	Feeding technique
[7]	2.45, 2.7	$1.02 \times 0.76 \times 0.03\ \lambda_0^3$ @ 2.45 GHz	1.5	3.4 @ 2.45 GHz	4.7 @ 2.45 GHz	Rubber	Microstrip
		$1.12 \times 0.84 \times 0.04\ \lambda_0^3$ @ 2.7 GHz		7 @ 2.7 GHz	5.1 @ 2.65 GHz	foam	Line
[8]	2.45, 5.8	$0.56 \times 0.50 \times 0.03\ \lambda_0^3$ @ 2.45 GHz	1.5	4.9 @ 2.45 GHz	4.1 @ 2.45 GHz	Rubber	Coaxial
		$1.33 \times 1.20 \times 0.08\ \lambda_0^3$ @ 5.80 GHz		5.1 @ 5.8 GHz	5.8 @ 5.8 GHz	foam	Cable
[17]	3.5, 5.8	$0.51 \times 0.51 \times 0.023\ \lambda_0^3$ @ 3.5 GHz	1.2	5 @ 3.55 GHz	2.8 @ 3.5 GHz	Wool	Microstrip
		$0.85 \times 0.85 \times 0.038\ \lambda_0^3$ @ 5.8 GHz		3.5 @ 5.8 GHz	3.5 @ 5.8 GHz	felt	Line
[18]	2.45, 5.5	$0.83 \times 0.75 \times 0.025\ \lambda_0^3$ @ 2.45 GHz	1.3	6.4 @ 2.45 GHz	2 @ 2.45 GHz	Felt	Coaxial
		$1.86 \times 1.69 \times 0.055\ \lambda_0^3$ @ 5.5 GHz		12 @ 5.5 GHz	5.6 @ 5.5 GHz		Cable
[22]	3.5, 4.9	$0.16 \times 0.16 \times 0.013\ \lambda_0^3$ @ 3.5 GHz	2.2	2.2 @ 3.5 GHz	4.4 @ 3.5 GHz	RT 5880	Coaxial
	5.4, 5.8	$0.33 \times 0.33 \times 0.026\ \lambda_0^3$ @ 4.9 GHz		3.05 @ 4.9 GHz	5.1 @ 4.9 GHz	Duroid	Cable
		$0.36 \times 0.36 \times 0.028\ \lambda_0^3$ @ 5.4 GHz		3.14 @ 5.4 GHz	5.4 @ 5.4 GHz		
		$0.39 \times 0.39 \times 0.03\ \lambda_0^3$ @ 5.8 GHz		3.2 @ 5.8 GHz	5.7 @ 5.8 GHz		
[23]	2.4, 3.51	$0.64 \times 0.64 \times 0.016\ \lambda_0^3$ @ 2.4 GHz	2.72	11 @ 2.4 GHz	1.1 @ 2.4 GHz	Leather	Coaxial
	4.69	$0.94 \times 0.94 \times 0.023\ \lambda_0^3$ @ 3.51 GHz		7 @ 3.51 GHz	0.9 @ 3.51 GHz		Cable
		$1.25 \times 1.25 \times 0.031\ \lambda_0^3$ @ 4.69 GHz		5 @ 4.69 GHz	2.1 @ 4.69 GHz		
This Work	**0.867, 0.915**	**$0.37 \times 0.38 \times 0.011\ \lambda_0^3$ @ 867 MHz**	**1.38**	3 @ 0.867 GHz	-1.3 @ 0.867 GHz	Rubber	Coaxial
		$0.35 \times 0.36 \times 0.011\ \lambda_0^3$ @ 915 MHz		3.5 @ 0.915 GHz	-0.6 @ 0.915 GHz	foam	cable

The designer of flexible textile antennas must take into account mechanical influences (such as crumpling, compression and bending), unwanted back-radiation absorbed by the wearer (which can reduce antenna efficiency and cause potential health threats when exceeding SAR limits), frequency detuning, degradation of performance, and so on. All these problems can be minimized if the designed structure shows a high body-antenna isolation.

In the last years, substrate integrated waveguide (SIW) technology has been exploited in the design of wearable and textile antennas, since antennas based on SIW cavities increase the antenna-body isolation (due to the resonant cavity structure and to the presence of a ground plane), ensure high flexibility [6], [7] with a low-profile planar structure, and can be designed with wideband/multiband operation [7], [8]. Moreover, they are particularly suitable for miniaturization since their size can be easily reduced by exploiting the symmetry of the electromagnetic field distribution of the cavity resonant modes [6], [7], [8], [9], [10], [11], [12], [13], [14], [15], [16], [17], [18].

Several wearable SIW antennas have been proposed in the literature ranging from UHF up to the C-band [6], [7], [8], [9], [10], [11], [12], [13], [14], [15], [16], [17], [18]. The vertical vias forming the cavity can be realized with embroidered conductive thread [9], or with metallized eyelets inserted into the textile substrate [6].

Most of the SIW antennas proposed so far have been designed to cover a single and narrow frequency band [6], [9], [10], [11], [12], [13], [14], [15], [16]. However, dual-band operation can be a desirable feature for wearable antennas in several application, such as LoRa [19], [20], [21] (working at 863-870 MHz in Europe and at 902-928 MHz in North America), WiFi and WLAN (around 2.4 GHz and 5.8 GHz), and WiMax (2.5 GHz and 3.5 GHz). In all these cases, SIW technology provides undeniable benefits, such as high isolation from the body, easy integration on garments, low cost, and compact realization.

Yet, only a few wearable SIW antennas with dual-band [7], [8], [17], [18] or multi-band [22], [23] behavior are available in the literature (see Table 1), wherein the required dual-band operation is achieved by exciting the higher order modes of the SIW cavity. The higher modes are excited using suitable geometries [7], [22], [23], tuning the feeding position [8], or using shorting vias [17], [18].

All the above configurations operate at 2.45 GHz or at higher frequencies (Table 1), whereas, to the best of the authors' knowledge, dual-band or multi-band operation in the lower part of the UHF band, where miniaturization is critical, is missing in the literature.

Moreover, in [7], [8], [17], [18], and [23], the frequency bands are strictly constrained by the resonant frequencies of the higher modes, intrinsically limiting the flexibility of these designs if they need to be employed at different frequencies for an arbitrary application. As a consequence, it is not a coincidence that each of the dual-band/triple-band configurations proposed so far has been tailored for the selected frequency bands: the wearable textile antenna proposed in [7] is designed for operation in the [2.4–2.48]-GHz Industrial, Scientific and Medical (ISM) band and in the [2.5–2.69]-GHz 4G LTE band; in [8] a wearable textile antenna is designed for optimal on-body performance in the 2.4 and 5.8 GHz ISM bands; in [17] a compact dual-band textile antenna operating in the 3.5 GHz WiMAX band and the 5.8 GHz ISM band is proposed; in [18] a dual-band textile

antenna for multiple-input multiple-output (MIMO) applications is designed to cover the 2.4 GHz ISM band and the 5-GHz WLAN band; finally, in [23], a wearable triple-band leather antenna is designed in the 2.4 GHz (ISM), 3.51 GHz (WiMAX) and 4.69 GHz (military applications) frequency bands.

Reconverting the previously described dual-band/triple-band SIW antennas [7], [8], [17], [18], [23] to different and arbitrary frequency bands could be feasible, but at the cost of a complicate rescaling of the structure. In fact, independently of the cavity size, suitable cavity modes ensuring good radiation properties cannot always be found to cover arbitrary frequency bands.

From the analysis reported in Table 1 it is also clear that a hypothetical scaling of the wearable antennas proposed in [7], [8], [17], [18], and [23] at sub-GHz frequencies, e.g. in the LoRa UHF bands, would results in large geometries, uncomfortable for the wearer.

The last multi-band SIW antenna [22] reported in Table 1 is instead a 4-ports full-mode circular SIW cavity which is split into four unequal quarter-mode SIW (QMSIW) cavities using two separating slots on the upper layer of the cavity. Each QMSIW cavity is separately fed by a coaxial probe and its (single) resonant frequency is tuned by a C-shaped slot of different dimensions in order to operate at wireless local area network bands: the first QMSIW works at 3.5 GHZ, the second QMSIW at 4.9 GHz, the third one at 5.4 GHz, and the last one at 5.8 GHz.

In this paper, a compact dual-band wearable antenna is presented. It is based on a rectangular eighth-mode substrate integrated waveguide (EMSIW) topology and prototyped using common textile materials. Specifically, starting from the antenna proposed in [16] that operates only in the European LoRa UHF band (the narrower one), we demonstrate the potential of the new configuration proposed here by designing a dual-band antenna that covers both the LoRa UHF bands (EU and USA), wherein ensuring a compact size is an important challenge.

Unlike the dual-band SIW antennas presented in the literature [7], [8], [17], [18], where both frequency bands depend on the size of the SIW cavity, the proposed design features a dual-band behaviour using a different operating principle for each of the two resonances, allowing improved flexibility in the frequency bands selection. Namely, one resonance is determined by the SIW cavity size through the excitation of its fundamental mode, whereas the other one depends on the length of a meandered slot cut in the upper wall of the cavity.

In Section II, we describe the design steps for obtaining two different and arbitrary working frequency bands. Then, the proposed procedure is applied to the design of an EMSIW antenna covering the two UHF LoRa bands centered at 867 MHz and at 915 MHz.

The antenna has been designed using CST Studio Suite, a reliable commercial software whose results can be considered equivalent to experiment for a wide range of applications [24], [25]. Then, a prototype of the LoRa antenna has been fabricated, tested, measured, and validated both in free-space and on-body, showing a very good agreement with simulated results and high robustness and isolation with respect to the human body coupling.

The miniaturization technique based on the symmetry of the SIW cavity fundamental mode leads to a size of $0.37 \times 0.38 \times 0.01\ \lambda_0^3$ at 915 MHz for the proposed antenna, providing reduced size with respect to the other wearable dual-band SIW antennas in the literature [7], [8], [17], [18] (see Table 1).

II. SIW ANTENNA DESIGN

In this section, we describe the general guidelines for the design of the proposed wearable EMSIW dual-band antenna. Then, without loss of generality, the design strategy is applied to the particular case of an EMSIW antenna operating in both UHF LoRa bands, the European one (863-870 MHz) and the North American one (902-928 MHz). The dielectric substrate employed for this specific design consists of a closed-cell rubber foam [6], [7], [8], [10], [15], [16], commonly used for the fabrication of protective clothing. The substrate thickness is 4 mm, and the dielectric permittivity, measured using the microstrip T-resonator method [26], is 1.38, with loss tangent $\tan\delta = 0.013$ at 900 MHz. The conductive material of the SIW (both for the ground plane and the top patch) has been realized using a 0.11 mm-thick adhesive copper-coated non-woven PET fabric, having a sheet resistivity equal to 0.14 Ω/square.

The antenna is fed by a 50 Ω SMA coaxial connector, whose position must be properly selected to obtain the desired input matching but paying attention to minimize undesired perturbations of the electromagnetic field distribution inside the cavity. It should be noted that the SMA connector could be obtrusive and uncomfortable for the wearer. However, since wearable antennas are usually integrated into jackets or garments, an adequate spacing (up to a few centimeters) is expected between the antenna and the wearer's body. On the other hand, if necessary, the SMA connector can be replaced by an UFL connector to obtain a thinner structure.

The design evolution of the SIW textile antenna toward the final EMSIW configuration is summarized in Fig. 1. The full-mode Square SIW cavity is reported in Fig. 1(a) together with the magnetic field distribution inside the cavity. The fundamental mode is the TM_{110} mode, whose resonant frequency can be computed by the well-known formula:

$$f_{110} = \frac{c}{2\pi\sqrt{\varepsilon_r \mu_r}} \left(\frac{\pi}{L_{SIW}}\right) \sqrt{2} \tag{1}$$

where L_{SIW} is the cavity side, c is the light speed in free-space and ε_r and μ_r are, respectively, the dielectric and magnetic permittivity of the material filling the cavity.

Following the SIW design guidelines given in [27] and [28], aiming to get a low attenuation constant and to

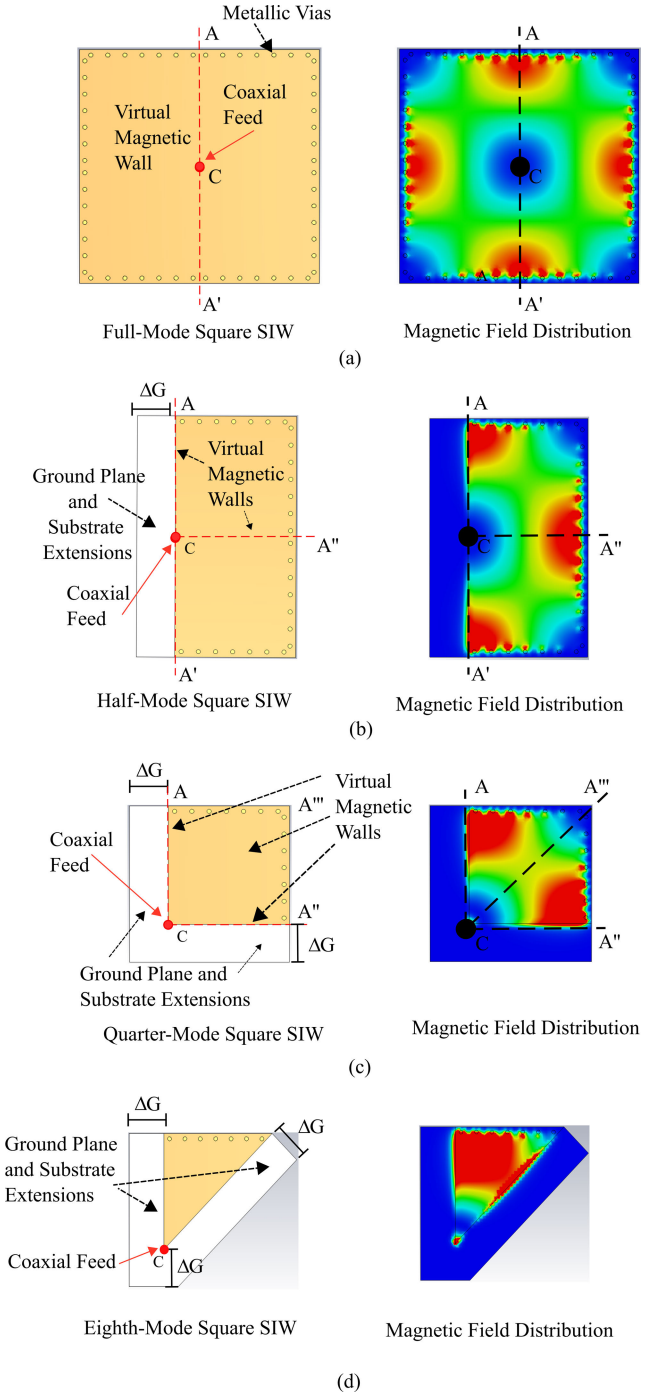

FIGURE 1. Design evolution of the SIW textile antenna: (a) full-mode square SIW and its magnetic field distribution; (b) half-mode SIW and its magnetic field distribution; (c) quarter-mode SIW and its magnetic field distribution; (d) eighth-mode SIW and its magnetic field distribution.

minimize the radiation leakage due to the apertures between two neighbouring vias, we consider that:

- the diameter R_H of the metal vias must be chosen small if compared with the free-space wavelength at the cavity operating frequency ($R_H/\lambda_0 \leq 0.1$);
- $D_H/R_H < 2.5$, with $D_H/R_H = 2$ being the recommended value, where D_H is the spacing between two adjacent vias.

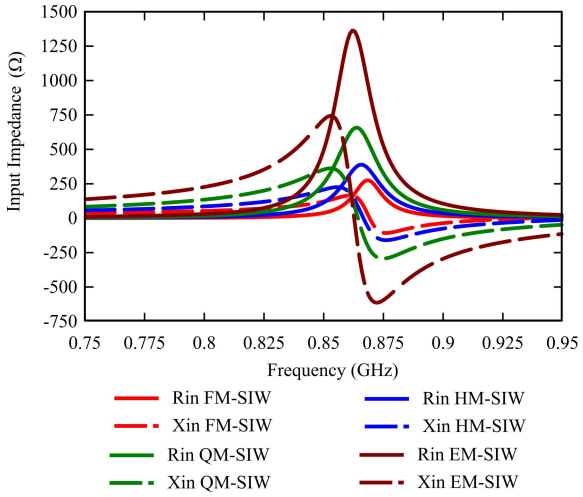

FIGURE 2. Input impedances of the SIW textile antenna evolving from full-mode square SIW to eighth-mode SIW.

When D_H and R_H are chosen complying with the previous rules, the gap between the metal vias is relatively small, approaching the condition of continuous metal wall, and the SIW cavity can be considered equivalent to a conventional metallic cavity.

Using (1), we first computed the resonant side of the square SIW cavity, corresponding to one of the required resonant frequencies of the dual-band antenna. Then, the magnetic field symmetry of the square cavity has been exploited to obtain the EMSIW cavity, as shown in Fig. 1(a-d). This figure depicts the fields distributions at 867 MHz for $L_{SIW} =$ 208 mm. Each of the SIW cavities indicated in Fig. 1(a-d) (full-mode, half-mode, quarter-mode and eighth-mode) is fed by a coaxial cable positioned at point C, which corresponds to the center of the full-mode SIW.

Looking at the magnetic field distribution of the full-mode cavity in Fig. 1(a), the field lines are symmetric along the plane ACA', which can be assumed as an equivalent perfect magnetic wall. Therefore, we can halve the full-mode cavity, cutting off the half of the cavity at the left of the ACA' plane, keeping a suitable ground plane extension ΔG. The result is the half-mode SIW (HMSIW) resonator depicted in Fig. 1(b) with its magnetic field distribution. The full-mode and half-mode cavities have approximately the same resonant frequency and the same field distributions at the fundamental mode, as apparent comparing the fields shown in Figs. 1(a) and 1(b). This is confirmed by the input impedance of the four SIW cavities listed in Fig. 1(a-d), which is reported in Fig. 2.

The HMSIW has been then further halved by exploiting the magnetic field symmetry along the plane indicated by the line CA'' in Fig. 1(b), obtaining the quarter-mode SIW resonator (QMSIW) shown in Fig. 1(c). Since the magnetic field of the QMSIW is symmetric along the plane CA''', it is finally halved to generate the eighth-mode SIW resonator (EMSIW) of Fig. 1(d).

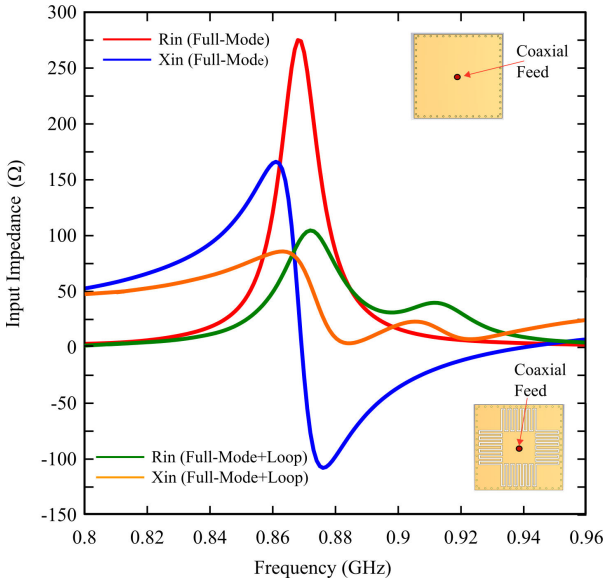

FIGURE 3. Frequency response of the full-mode SIW cavity with and without a meandered loop cut in the top patch.

The full-mode SIW cavity of Fig. 1(a) works as a lossy cavity around 867 MHz, the resonant frequency of its fundamental TM_{110} mode. In Fig. 3 the input impedance for $L_{SIW} = 208$ mm is reported for a centered feeding (red and blue curves). It is worth noting that the full-mode SIW is not matched when the coaxial feed is positioned at its center, with a peak of the real part of the input impedance equal to 275 Ω at the resonant frequency of the cavity.

To obtain a dual-band behavior, we added a meandered slotted loop cut on the top patch of the SIW cavity. The total length of the loop L_{LOOP} will determine the second resonant frequency of the structure. In Fig. 3 the input impedance of the SIW cavity with the meandered loop is reported for a centered feeding (green and orange curves). The green and orange curves in Fig. 3 have been computed for $L_{SIW} = 208$ mm and $L_{LOOP} = 386.4$ cm. In this case, the loop length is selected to provide a resonance close to that of the SIW cavity (as requested by the UHF LoRa bands), while paying attention to preserve the magnetic field symmetry for the subsequent reduction to the EMSIW configuration. Indeed, the meandered loop introduces a further resonance, but also modifies the resonant frequency of the SIW fundamental mode and the electromagnetic field distribution inside the cavity. The latter is shown in Figs. 4 and 5, wherein the electric and magnetic field distributions are plotted both at the resonant frequency of the SIW cavity (Fig. 4(a) and 5(a)) and at the resonant frequency of the meandered loop (Figs. 4(b) and 5(b)). Also the position of the coaxial feed has an important role in the SIW antenna design since it strongly influences both the input matching and the electromagnetic field distribution inside the cavity. The appropriate choice of the feeding point will be discussed in Section IV-E.

From the above considerations and from the simulations reported in Fig. 3, it is apparent that to obtain the

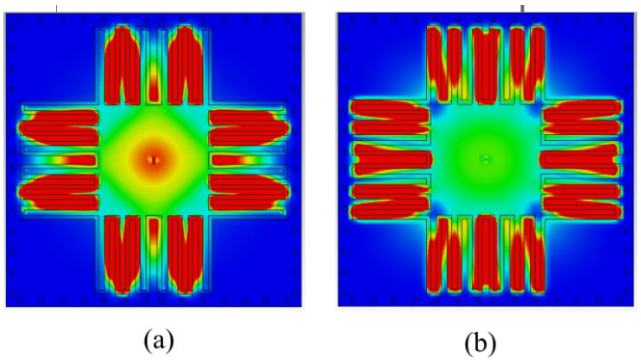

FIGURE 4. Electric field distribution inside the full-mode cavity at (a) the resonant frequency of the SIW cavity; (b) the resonant frequency of the meandered loop.

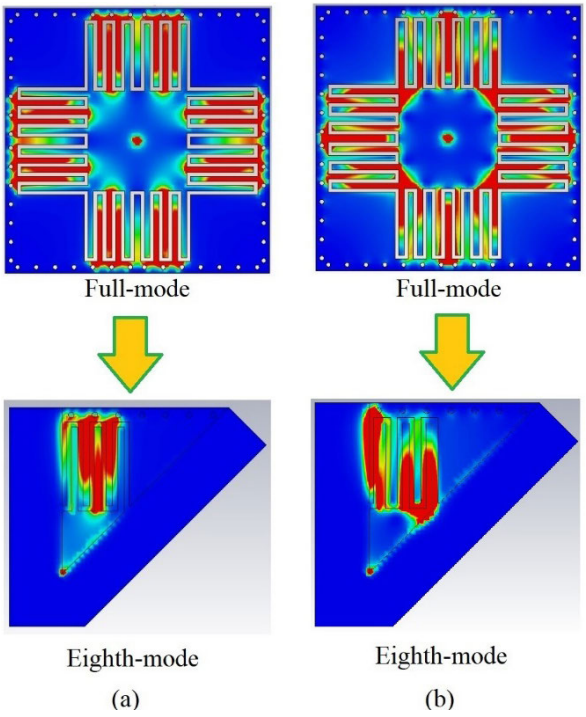

FIGURE 5. Magnetic field distribution inside the cavity at (a) the resonant frequency of the SIW cavity; (b) the resonant frequency of the meandered loop.

two resonances at the desired LoRa frequencies (867 MHz and 915 MHz) we need to perform some optimizations, adjusting the cavity size, the feeding point, and the loop length.

At this point, since the meandered loop does not affect the magnetic field symmetry (see Fig. 5), before tuning the operating frequencies we applied to the cavity with the meandered loop the same procedure described in Fig. 1, to obtain the reduced-size EMSIW configuration reported in Fig. 6(a).

The EMSIW cavity radiates through the lateral apertures, therefore an adequate extension ΔG of both dielectric substrate and ground plane must be kept in correspondence to the magnetic wall cuts, as explicitly indicated in

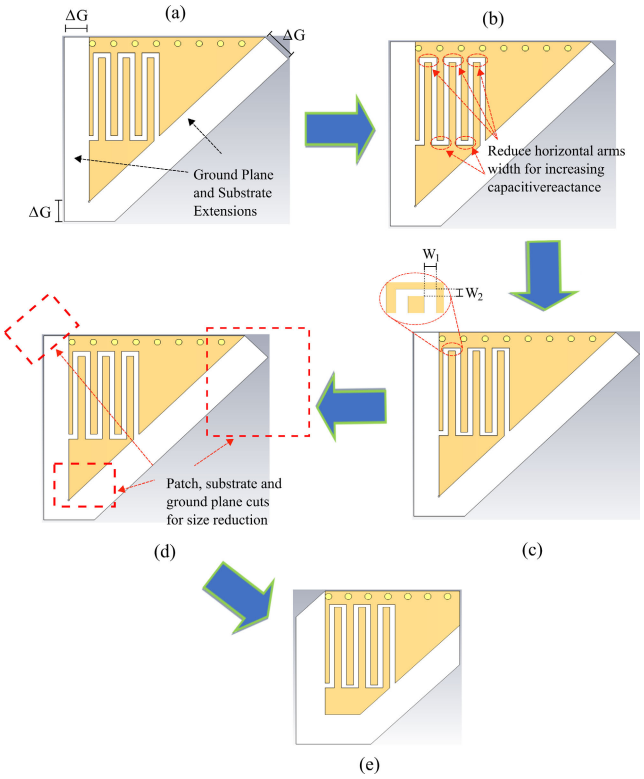

FIGURE 6. Main steps of the design process: (a) EMSIW ground plane and substrate extensions; (b) meandered loop horizontal arms thinning to increase the capacitive reactance of the EMSIW; (c) zoom of the meandered line with different arms widths; (d) cuts in the EMSIW structure to reduce the antenna size; (e) final designed EMSIW antenna.

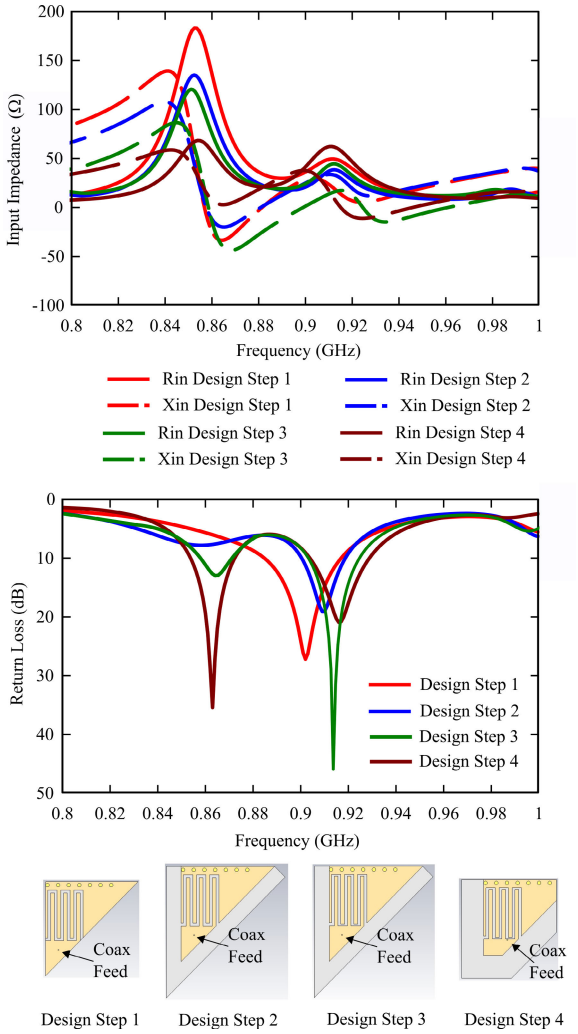

FIGURE 7. Input impedance and return loss of the SIW antenna at the main design steps described in Fig. 6.

Figs. 1(d) and 6(a). These extensions improve the on-body antenna performance, increasing its isolation and robustness with respect to the proximity with the human body. A larger ground plane results in a greater shielding effect, but can strongly increase the antenna dimension, therefore a suitable trade-off has been found between antenna size and robustness. The details on the choice of ΔG and on its effect on the antenna performance are discussed in Section IV-D.

The main design criteria for the dual-band EMSIW antenna are described in the following:

1) An appropriate feeding point for the coaxial cable must be selected, aiming to minimize the perturbation of the electromagnetic field inside the cavity and to obtain a satisfactory input matching of the antenna.
2) Since the insertion of the meandered slot introduces a significant inductive reactance, a capacitive counterpart must be taken into account for the input impedance of the EMSIW antenna to improve its matching with the coaxial feeding. This can be achieved by reducing the width of the horizontal arms of the meandered slot, as described in Figs. 6(b) and 6(c).
3) The cavity size and the lengths of the vertical arms of the meandered slot must be tuned to obtain the antenna dual-band behavior at the LoRa frequencies.

The extensions ΔG (see Fig. 1) of both dielectric substrate and ground plane have been set to 20 mm to adequately shield the antenna from the body. The EMSIW upper and lower wedges have been cut off to reduce the antenna size as detailed in Fig. 6(d), since the antenna behavior is not affected by these layout modifications.

In Fig. 7 the simulated performance of the SIW antenna is reported for each of the main design steps summarized in Fig. 6. At the first step, the SIW antenna has no ground plane and substrate extensions and it is fed by a coaxial cable positioned at an arbitrary point of the upper patch below the meandered slot. In this case, the feed point is centered with respect to the antenna horizontal width. The input impedance shows a relatively high inductive imaginary part, due to the presence of the meandered slot, the return loss is not satisfying and the antenna gain is very low (as accurately described in Section IV-D). In the second design step, an extension $\Delta G = 20$ mm of both dielectric substrate and ground plane is added in correspondence to the magnetic wall cuts, improving

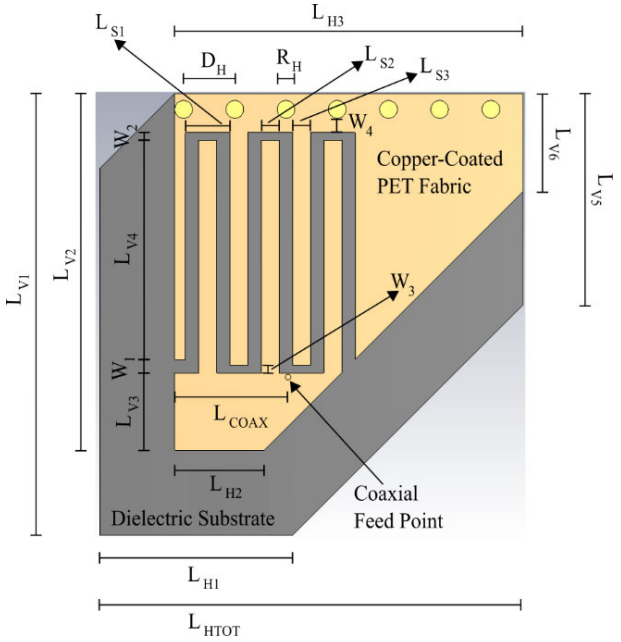

FIGURE 8. Layout of the designed SIW antenna. $L_{V1} = 125$ mm, $L_{HTOT} = 120$ mm, $L_{V2} = 101$ mm, $L_{V3} = 21.9$ mm, $L_{V4} = 62$ mm, $L_{V5} = 60$ mm, $L_{V6} = 27.9$ mm, $L_{H1} = 54.6$ mm, $L_{H2} = 25.4$ mm, $L_{H3} = 98.5$ mm, $D_H = 14$ mm, $R_H = 7$ mm, $L_{S1} = 12.6$ mm, $L_{S2} = 5$ mm, $L_{S3} = 5$ mm, $W_1 = 3.8$ mm, $W_2 = 2.2$ mm, $W_3 = 2.2$ mm, $W_4 = 4$ mm, $L_{COAX} = 32$ mm.

the antenna gain and its on-body performance (the choice of this value for ΔG will be explained in Section IV-D). The results of the input impedance and return loss simulations for this case are improved with respect to the first design step, with a better input matching, but the inductive imaginary part is still too high. Therefore, in the third design step a capacitive contribution has been added to the SIW input impedance by reducing the width of the horizontal arms of the meandered slot. As a result, the input impedance shows an acceptable behavior of its imaginary part, and the return loss is strongly improved. In the fourth design step, the SIW upper and lower wedges have been cut off to reduce the antenna size and the coaxial feed has been moved to an appropriate position to obtain a suitable input matching within the two working frequency bands, ensuring the requested dual-band behavior.

Following the design guidelines described above, we obtained the EMSIW antenna shown in Fig. 8, in which all the relevant geometric parameters are clearly indicated. The planar size is 12.5×12 cm^2, providing a compact implementation at UHF frequencies (see also Table 1). The resulting EMSIW antenna produces a broadside far-field pattern, radiating away from the wearer through the open side walls of the cavity.

III. SIMULATIONS AND RESULTS

Wearable antennas performance can be severely degraded by the coupling with the human body, an extremely lossy and non-homogeneous material. Moreover, the distance between the wearable antenna and the user modifies unpredictably

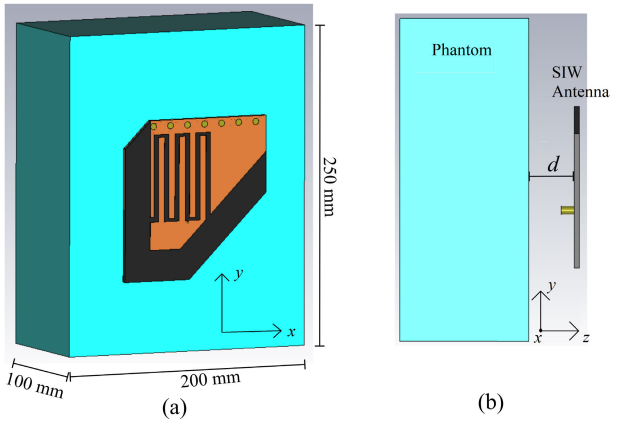

FIGURE 9. 3D view (a) and side view (b) of the designed EMSIW antenna with the single-layer phantom model used in the CST numerical simulations.

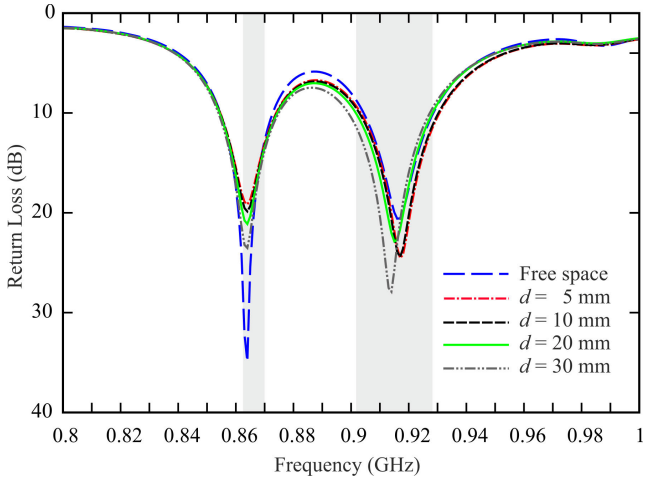

FIGURE 10. Simulated frequency response of the designed SIW antenna in free-space and for different values of the distance d between the antenna and the single-layer phantom model.

during typical operating conditions. Therefore, adequate countermeasures must be adopted to obtain a performance as stable and robust as possible regardless of the distance with respect to the human body, aiming to achieve a good antenna isolation. We used a numerical phantom in the CST simulations to study the effect of the body proximity on the antenna performance. This phantom consists of a simplified single layer with muscle-like dielectric properties around 900 MHz ($\varepsilon_r = 56.6$, $\sigma = 1.33$ S/m) and with a size of $250 \times 200 \times 100$ mm^3 [16], [29], as depicted in Fig. 9.

In Fig. 10, the simulated antenna return loss is shown for different spacings d between the antenna and the body phantom and compared with the performance of the antenna deployed in free-space. The minimum distance between the antenna and the phantom is set to $d = 5$ mm, because the feeding SMA connector prevents the antenna to be attached to the phantom. These results show that the simulated return loss is substantially independent of d, ensuring a good input matching also in the case of unavoidable random movements

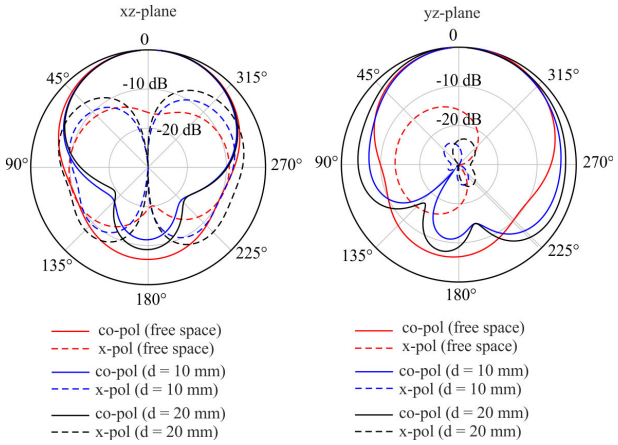

FIGURE 11. Simulated normalized far-field pattern of the designed SIW antenna at 867 MHz.

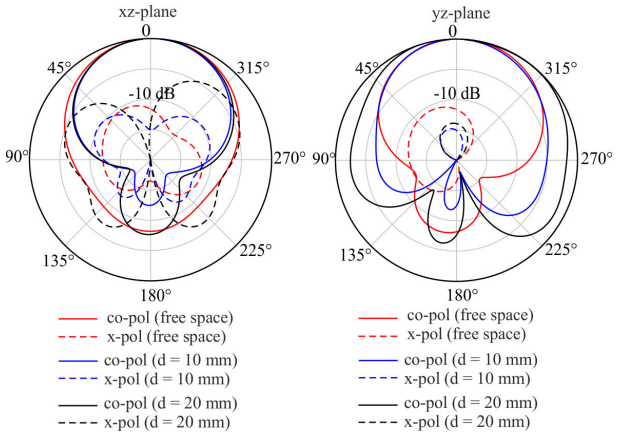

FIGURE 12. Simulated normalized far-field pattern of the designed SIW antenna at 915 MHz.

TABLE 2. Simulated directivity, gain, and efficiency of the designed EMSIW antenna.

	D (dBi) 867, 915 MHz	G (dBi) 867, 915 MHz	η (%) 867, 915 MHz
Free-space	4.93, 5.05	-1.12, -0.80	25, 26
$d = 5$ mm	5.47, 5.59	-1.12, -1.06	22, 22
$d = 10$ mm	5.65, 5.74	-0.70, -0.98	23, 21
$d = 20$ mm	5.32, 5.92	-1.40, -0.50	21, 23
$d = 30$ mm	5.26, 5.72	-1.54, -0.85	21, 22

of the wearer, always maintaining the complete coverage of the UHF LoRa frequency bands, highlighted by the two grey bands in Fig. 10.

Figs. 11 and 12 display the simulated normalized far-field pattern at 867 MHz and 915 MHz, when the antenna radiates in free-space or in proximity of the human body (for d = 10 mm and 20 mm), respectively.

In Table 2 the antenna maximum directivity D, gain G, and efficiency η are reported at the two LoRa center frequencies (867 MHz and 915 MHz) for the antenna deployed in free-space and at different spacings from the phantom. Despite

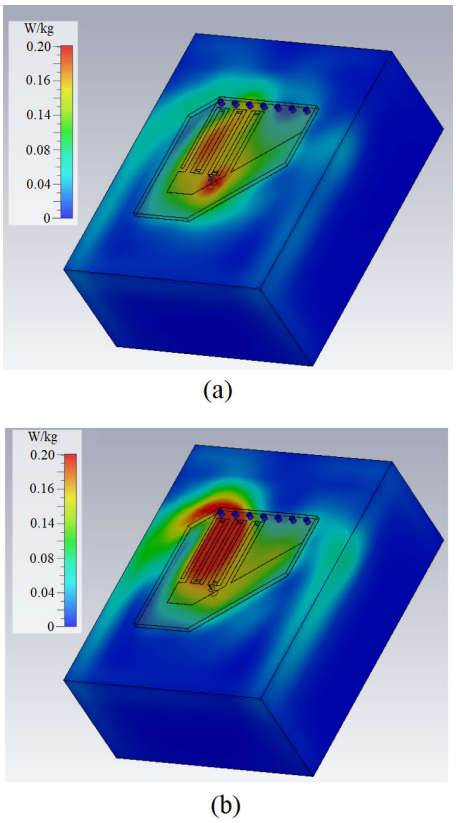

FIGURE 13. Simulated SAR values for the SIW antenna placed at 5 mm from the phantom at a) 868 MHz; b) 915 MHz.

the high dissipations due to the human body proximity, the gain values are satisfactory in the whole operating frequency band. The robustness of the radiated field with respect to the human body coupling can be considered excellent for LoRa applications (see Figs. 11 and 12). The total efficiency ranges from 21% to 26% for varying d in the range [0 - 30 mm], which is a good value for textile wearable antennas in the lower part of the UHF frequency band, especially considering the low-cost rubber foam and textile conductive fiber used to manufacture the antenna.

In order to estimate the radiation absorbed by the human tissue, the SAR values are computed using CST Studio Suite for the layout described in Fig. 9, wherein the human body has been modeled with a single layer phantom. The SAR levels are shown in Fig. 13. When the SIW antenna is placed at 5 mm from the human tissue, the calculated maximum SAR value for 500 mW input power is lower than 0.2 W/kg, averaged over 1 g of tissue, for both working frequencies of 868 and 915 MHz. SAR values are therefore well below the maximum limit of 1.6 W/kg averaged over 1 g of tissue [10], [30]. Actually, this result was expected, since most of the radiation is directed away from the body thanks to the presence of the ground plane and to the vias of the SIW structure.

Finally, one of the critical aspects for wearable antennas, which will suffer from arbitrary bending and deformations

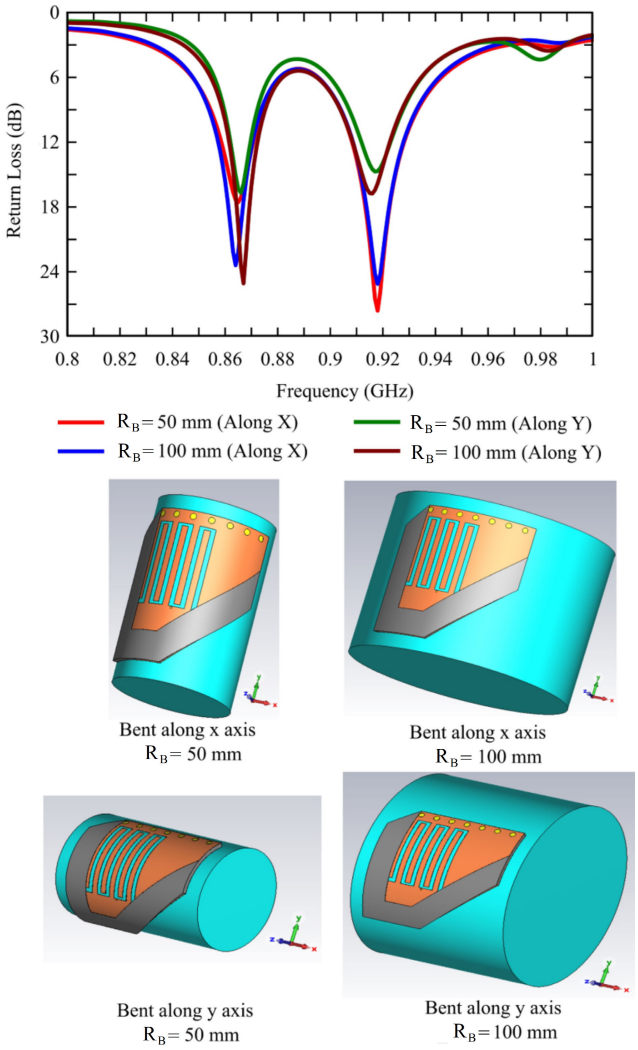

FIGURE 14. Simulated return loss of the SIW antenna for different bending conditions.

due to the natural wearer's movements, is flexibility. Therefore, in Fig. 14 we report the performance of the proposed antenna both for a horizontal (along x-axis) and a vertical bending (along y-axis) for two different bending radii: $R_B = 50$ mm, which represents a bending around a human arm, and $R_B = 100$ mm, which represents a bending around a human leg. The presented results show a good robustness of the SIW antenna with respect to bending, with only a little shift in the frequency response (compared with the results of the flat SIW shown in Fig. 10) even for a relatively strong bending (50 mm).

IV. PARAMETRIC ANALYSIS

A parametric analysis of the designed antenna is presented in this section, considering the main design variables and their effect on the antenna behavior: the position of the meander loop, the number of U turns of the meander loop, the width of the meander loop, the extensions of the ground plane and dielectric substrate, and the position of the coaxial feed.

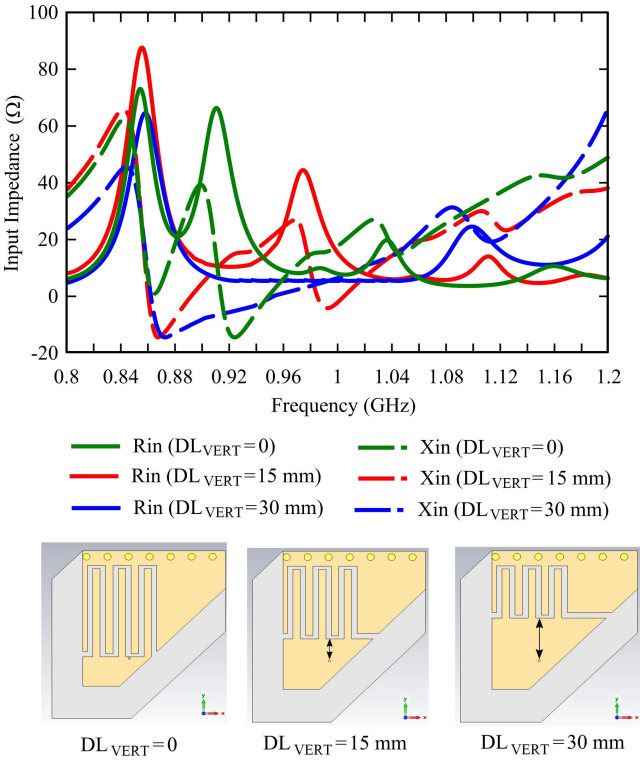

FIGURE 15. Simulated input impedance of the SIW antenna for different positions of the meander loop.

A. MEANDER LOOP POSITION

In Fig. 15 the simulated input impedance of the SIW antenna is shown for three different positions of the meander loop, with DL_{VERT} indicating the distance between the lower part of the meander loop and the feeding point. For increasing values of DL_{VERT} the total length of the meander loop becomes smaller, therefore the resonant frequency of the loop shifts towards higher frequencies, whereas the resonant frequency of the cavity remains substantially unchanged. The optimal choice for DL_{VERT} corresponds to the value $DL_{VERT} = 0$ (i.e., the layout of the final antenna shown in Fig. 8), which translates the resonant frequency of the loop close to the desired operating frequency of the antenna (915 MHz in our case).

B. MEANDER LOOP U TURNS

Fig. 16 reports the simulated input impedance of the SIW antenna for different numbers of U turns of the meander loop. The behavior is similar to the one shown in Fig. 15. In fact, as the number of U turns increases, the total length of the meander loop becomes bigger, shifting the resonant frequency of the loop towards lower frequencies, whereas the resonant frequency of the cavity remains substantially unchanged. The meander loop with 3 turns is the one chosen for the final antenna layout shown in Fig. 8.

C. MEANDER LOOP WIDTH

In Fig. 17 the return loss of the SIW antenna for different widths W_1 (see Fig. 8) of the meandered slot is shown. The

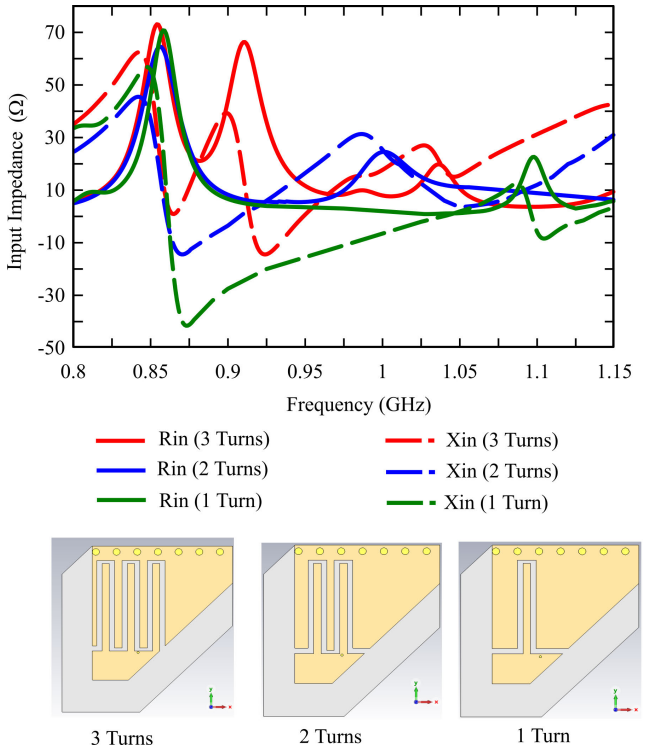

FIGURE 16. Simulated input impedance of the SIW antenna for different numbers of U turns of the meander loop.

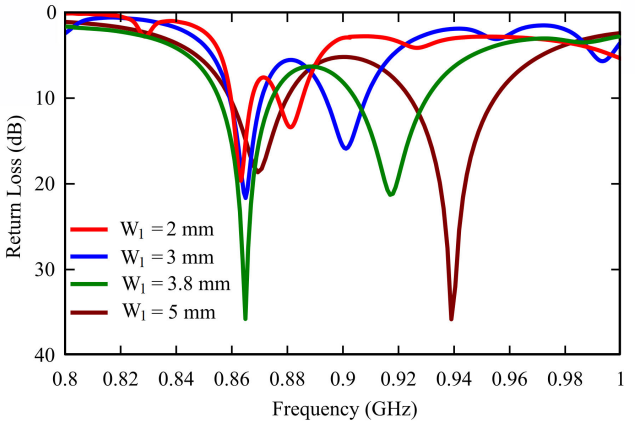

FIGURE 17. Simulated return loss of the SIW antenna for different widths of the meander loop.

resonant frequency of the meandered slot is tuned by its width, which slightly modifies also the resonant frequency of the cavity. Both resonant frequencies are shifted to higher frequencies for increasing values of W_1. Increasing W_1 also modifies the input impedance of the structure, since a thinner slot corresponds to higher values of the input impedance. As shown in the plot, the optimal value of $W_1 = 3.8$ mm has been chosen for the final antenna layout.

D. GROUND PLANE AND SUBSTRATE EXTENSIONS

The choice of the ground plane and dielectric substrate extensions ΔG (Fig. 1) plays a significant role in the design of the

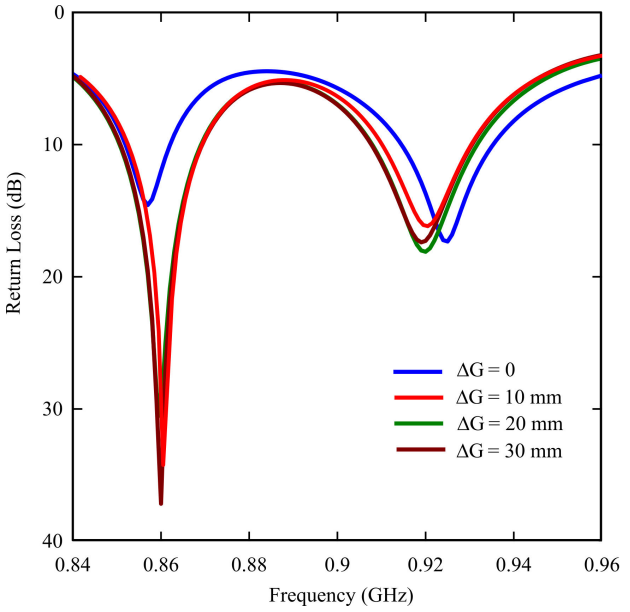

FIGURE 18. Simulated return loss of the SIW antenna deployed at 5 mm from the phantom for different values of the ground plane and substrate extensions ΔG.

SIW antenna for on-body applications. In fact, the ground plane shields the antenna from the human body and, as a result, a large ground plane extension improves the antenna robustness and isolation at the cost of larger antenna size. On the other hand, a SIW structure with a small ground plane extension will offer extremely poor on-body performance, with a low gain and an increase of the body absorption (i.e., a higher SAR level). An appropriate extension ΔG of both the ground plane and the dielectric substrate should be chosen during the antenna design to achieve a satisfying trade-off between antenna size and desired performance, robustness and isolation. In Fig. 18 the return loss of the antenna deployed at 5 mm from the phantom is shown for different values of the substrate and ground plane extensions ΔG. A reasonable trade-off between antenna size and robustness can be achieved when ΔG becomes larger than 0.15 λ_0 [10], wherein λ_0 is the free-space wavelength at the working frequency. In Fig. 19 the simulated gain of the SIW antenna deployed at 5 mm from the phantom is reported for different values of ΔG. When $\Delta G = 0$, the antenna is relatively small but the gain at the two operating frequencies is below -5 dBi, which is an extremely low gain even for on-body applications. On the other hand, for $\Delta G = 30$ mm, the antenna becomes larger but the gain value settles at -0.5 dBi, a satisfying value for a wearable antenna in the lower range of the UHF frequencies. Figure 20 shows the simulated far-field pattern at the two operating frequencies (867 MHz and 915 MHz) of the SIW antenna deployed at 5 mm from the phantom for $\Delta G = 0$ and $\Delta G = 20$ mm. It is pretty clear that the far-field is not acceptable for $\Delta G = 0$, because of the high values of the cross-polar component and back-radiation, and of the peak gain directed far from the broadside direction.

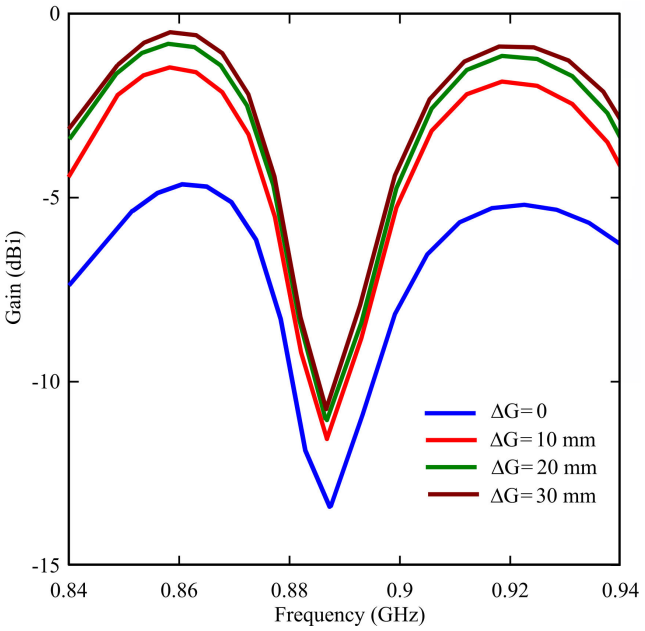

FIGURE 19. Simulated gain of the SIW antenna deployed at 5 mm from the phantom for different values of the ground plane and substrate extensions ΔG.

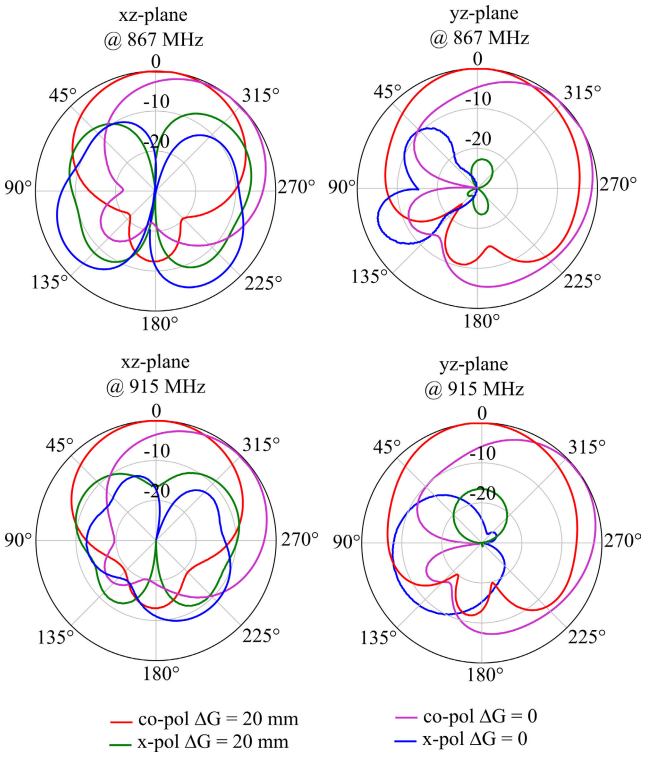

FIGURE 20. Simulated far-field Pattern at the two operating frequencies of the SIW antenna deployed at 5 mm from the phantom for ΔG = 0 (no extensions for ground plane and substrate) and ΔG = 20 mm (design value).

An appropriate choice of the ground plane and substrate extensions ΔG could stabilize the radiation efficiency and the far-field pattern. In our case, the optimal compromise between antenna performance and size can be reached for ΔG = 20 mm, resulting in a very good input matching, a gain of about -1 dBi for both operating frequencies, and a satisfying radiation pattern.

E. COAXIAL FEED POSITION

The position of the coaxial feed strongly influences both the siw input matching and the electromagnetic field distribution inside the cavity.

The reference system for the parametric variation of the coaxial feed position (X_0, Y_0) is shown in Figure 21(a), where the red circle corresponds to (0, 0). In Figure 21(b), the return loss of the antenna is reported for different values of the horizontal position of the coaxial feed X_0, with Y_0 fixed to 0. The input matching is good for $|X_0| < 10$ mm and deteriorates when the coaxial feed approaches the patch borders. Figure 21(c) shows the return loss for different values of the vertical position of the coaxial feed Y_0, with X_0 fixed to 0. The input matching can be improved by a suitable choice of Y_0, with $Y_0 \leq 0$, whereas it rapidly degrades for positive values of Y_0. This means that the feed must be positioned below the meandered slot in order to obtain an acceptable input matching of the SIW antenna, whereas positioning the feed along the vertical arm of the meandered slot strongly degrades the antenna behavior.

This is confirmed also looking at the electric energy density distribution inside the cavity reported in Fig. 22. Figs. 22 (a) and (b) show the electric energy density distribution at the two working frequencies of 868 MHz and 915 MHz when the coaxial feed is positioned below the meandered slot at the position (0, 0). At 868 MHz (resonant frequency of the SIW cavity), the cavity is correctly excited, and at 915 MHz (resonant frequency of the meandered slot), the slot is correctly excited, which means that the dual-band antenna is properly working. On the other hand, Figs. 22 (c) and (d) show the electric energy density distribution at the two working frequencies of 868 MHz and 915 MHz when the coaxial feed is positioned along the vertical arm of the meandered slot at the position (0, 20). It is apparent that the cavity is not excited at its working frequency of 868 MHz, and also the meandered slot has a non-uniform excitation at its working frequency of 915 MHz. Therefore, we can conclude that the coaxial feed can be positioned only in the region below the meandered slot (indicated in Fig. 22(e) as matching region), because this choice ensures a very good input matching and does not perturb the electric field inside the cavity within the whole operating frequency band.

V. EXPERIMENTAL VERIFICATION

To experimentally assess the performance of the proposed EMSIW antenna, a prototype has been manufactured (Fig. 23). The SIW vias have been realized using metallic eyelets. This prototype has been measured both in free-space and in the presence of the human body (both with the help of

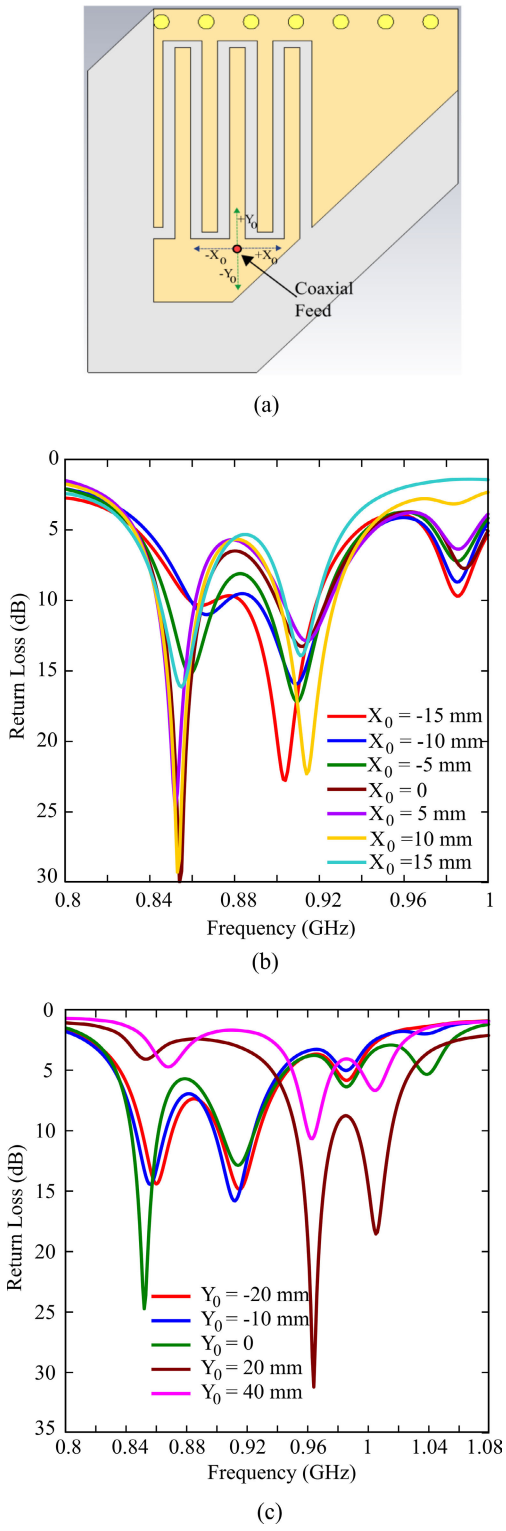

FIGURE 21. (a) Layout of the antenna with reference system for coaxial feed horizontal (X_0) and vertical (Y_0) positions. The red circle corresponds to $X_0 = 0$ and $Y_0 = 0$; (b) Simulated return loss of the SIW antenna for different values of the horizontal position X_0 of the coaxial feed; (c) Simulated return loss of the SIW antenna for different values of the vertical position Y_0 of the coaxial feed.

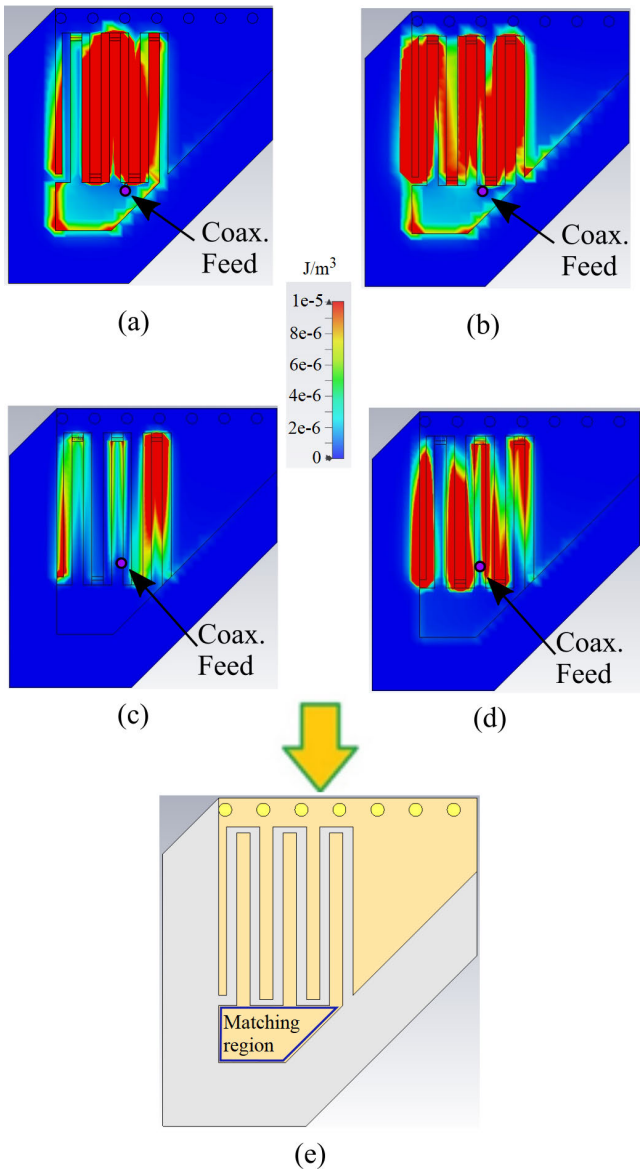

FIGURE 22. (a) Electric energy distribution inside the cavity at 868 MHz for the coaxial feed positioned below the meandered slot; (b) Electric energy distribution inside the cavity at 915 MHz for the coaxial feed positioned below the meandered slot; (c) Electric energy distribution inside the cavity at 868 MHz for the coaxial feed positioned along the vertical arm of the meandered slot; (d) Electric energy distribution inside the cavity at 915 MHz for the coaxial feed positioned along the vertical arm of the meandered slot; (e) Layout of the SIW antenna showing the matching region.

a volunteer and using a liquid phantom). The measurement setup is shown in Fig. 24.

The frequency response of the EMSIW antenna prototype, its far-field pattern, and its gain have been measured using the Anritsu MS46322B two-port vector network analyzer (VNA) and a gain calibrated test antenna (model HyperLOG 7060 by AARONIA AG) (see Fig. 24(a)). The HyperLOG 7060 antenna has been connected to a broadband low noise pre-amplifier (LNA) (model ZX60-83LN-S+ by Minicircuits) to improve the sensitivity of the measurement. The gain of the LNA has been previously measured using the VNA to obtain a reliable estimation of the EMSIW antenna gain.

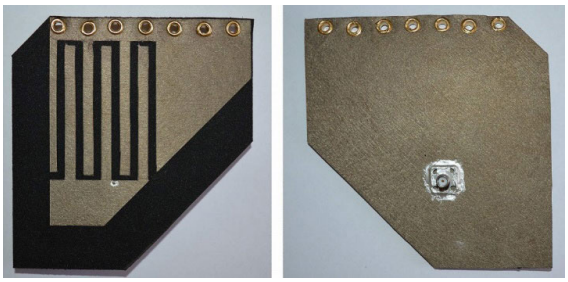

FIGURE 23. Front view and back view of the designed SIW antenna prototype.

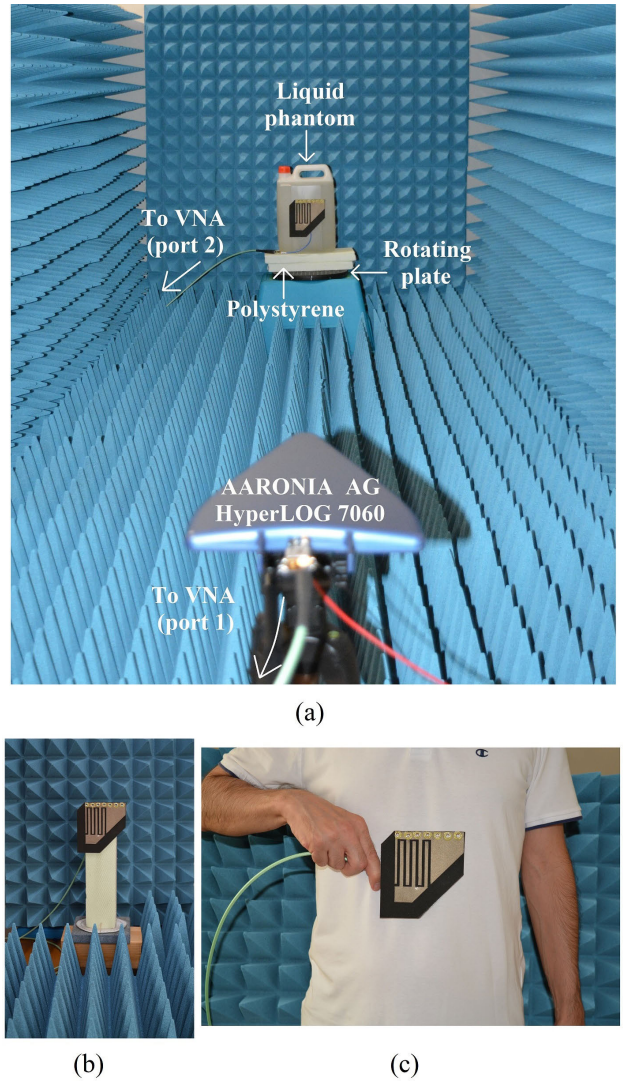

FIGURE 24. Measurement setup for the designed EMSIW antenna prototype in an anechoic environment: (a) the antenna is placed on a synthetic liquid phantom; (b) antenna mounted on a polystyrene support for free-space measurements; (c) antenna in proximity of a real human body (b).

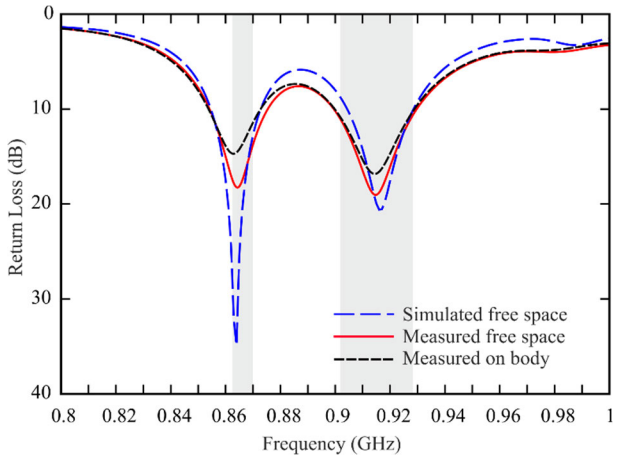

FIGURE 25. Simulated and measured frequency response of the designed SIW antenna in free-space and on body.

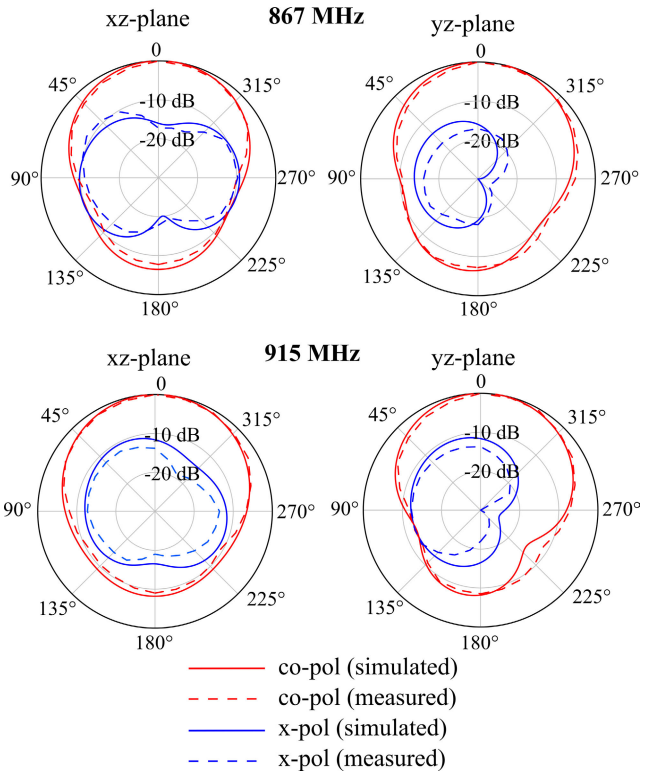

FIGURE 26. Far-field pattern of the manufactured prototype in free-space.

In Fig. 25, the measured return loss of the antenna, both in free-space and when it is close to the human-body (the average estimated d in Fig. 24(c) is about 10 mm), is reported and compared with the simulated results in free-space. A good agreement between simulation and measurement and a high robustness with respect to the human body can be observed (compare also with simulations in Fig. 10).

The far-field pattern and gain of the antenna in proximity of the liquid body phantom have been computed using the measurement setup in Fig. 24(a). The distance of the antenna from the liquid phantom has been set to about 20 mm, which is the minimum spacing required to connect the F-SMA of the antenna to a right-angle M-F SMA connector.

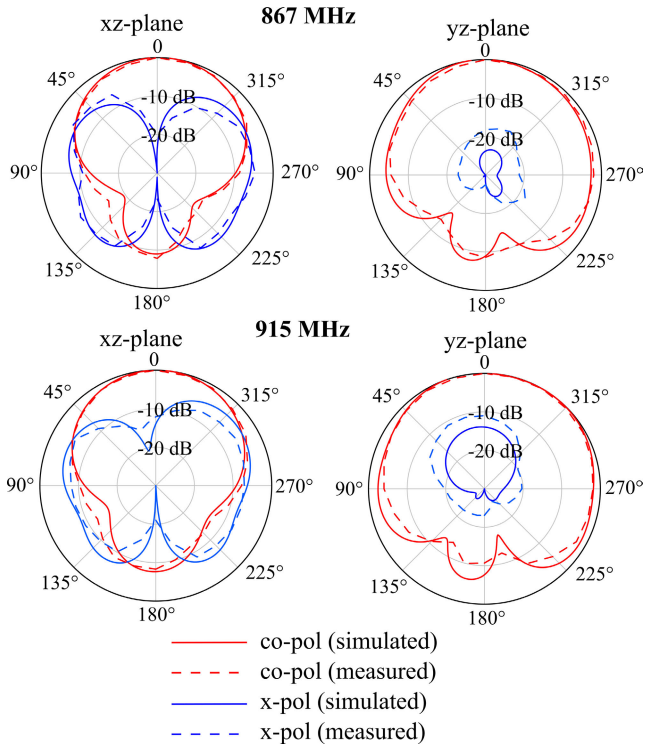

FIGURE 27. Far-field pattern of the manufactured prototype in proximity to the liquid body phantom (d = 20 mm).

The far-field pattern and gain in free-space have been computed in the same environment of Fig. 24(a), but without the liquid phantom and with the antenna mounted on a polystyrene support (as shown in Fig. 24(b)).

The measured gain of the antenna radiating in free-space at 867 MHz and 915 MHz is -0.9 dBi and -0.7 dBi, respectively. The measured gain of the antenna placed in proximity of the liquid body phantom at 867 MHz and 915 MHz is -1.3 dBi and -0.6 dBi, respectively. As apparent from comparison with simulated results in Table 2, a good agreement between simulated and measured gain is observed.

Finally, in Fig. 26 and 27 we show the comparison between simulated and measured far-field pattern in free-space (Fig. 24(b)) and with the antenna at 20 mm from the liquid phantom (Fig. 24(a)). The agreement is still very good.

VI. CONCLUSION

In this work, we exploited the SIW technology to design a novel textile dual-band antenna configuration. An eighth-mode SIW antenna, covering both UHF LoRa bands, has been obtained using the symmetry of the electromagnetic field of a full-mode square cavity, achieving a significant miniaturization, which is an important feature for wearable applications, mainly at UHF. Specifically, more than 45% planar size reduction with respect to similar state-of-the-art dual-band SIW antennas available in the literature has been obtained, allowing a compact and comfortable realization also in the lower part of the UHF band. Improved flexibility and frequency scalability can be achieved with the proposed configuration, since the two operating frequencies are not constrained by the resonant frequencies of the higher order modes of the SIW cavity, but rely on different operating principles. Namely, one resonance is determined by the SIW cavity size through the excitation of its fundamental mode, the other one depends on the length of a meandered slot cut in the upper wall of the cavity.

We demonstrated both with simulations and measurements that the selected SIW architecture provides very good isolation from the human body and high robustness with respect to the antenna-body distance variation. Finally, the EMSIW structure can be realized with a low-cost procedure, only requiring minimal patterning and embroidery.

REFERENCES

[1] P. S. Hall and Y. Hao, *Antennas and Propagation for Body-Centric Wireless Communications*. Norwood, MA, USA: Artech House, 2006.
[2] B. Latré, B. Braem, I. Moerman, C. Blondia, and P. Demeester, "A survey on wireless body area networks," *J. Wireless Netw.*, vol. 17, no. 1, pp. 1–18, 2011.
[3] I. Locher, M. Klemm, T. Kirstein, and G. Trster, "Design and characterization of purely textile patch antennas," *IEEE Trans. Adv. Packag.*, vol. 29, no. 4, pp. 777–788, Nov. 2006.
[4] L. Zhang, Z. Wang, D. Psychoudakis, and J. L. Volakis, "E-fiber electronics for body-worn devices," in *Proc. 6th Eur. Conf. Antennas Propag. (EUCAP)*, Prague, Czech Republic, Mar. 2012, pp. 760–761.
[5] T. Kaufmann, I. M. Fumeaux, and C. Fumeaux, "Comparison of fabric and embroidered dipole antennas," in *Proc. 7th Eur. Conf. Antennas Propag. (EuCAP)*, Gothenburg, Sweden, Apr. 2013, pp. 3252–3255.
[6] R. Moro, S. Agneessens, H. Rogier, and M. Bozzi, "Wearable textile antenna in substrate integrated waveguide technology," *Electron. Lett.*, vol. 48, no. 16, pp. 985–987, Aug. 2012.
[7] S. Lemey, F. Declercq, and H. Rogier, "Dual-band substrate integrated waveguide textile antenna with integrated solar harvester," *IEEE Antennas Wireless Propag. Lett.*, vol. 13, pp. 269–272, 2014.
[8] S. Agneessens and H. Rogier, "Compact half diamond dual-band textile HMSIW on-body antenna," *IEEE Trans. Antennas Propag.*, vol. 62, no. 5, pp. 2374–2381, May 2014.
[9] T. Kaufmann and C. Fumeaux, "Wearable textile half-mode substrate-integrated cavity antenna using embroidered vias," *IEEE Antennas Wireless Propag. Lett.*, vol. 12, pp. 805–808, 2013.
[10] C. S. Agneessens, S. Lemey, T. Vervust, and H. Rogier, "Wearable, small, and robust: The circular quarter-mode textile antenna," *IEEE Antennas Wireless Propag. Lett.*, vol. 14, pp. 1482–1485, 2015.
[11] M. E. Lajevardi and M. Kamyab, "Ultraminiaturized metamaterial-inspired SIW textile antenna for off-body applications," *IEEE Antennas Wireless Propag. Lett.*, vol. 16, pp. 3155–3158, 2017.
[12] Y. Hong, J. Tak, and J. Choi, "An all-textile SIW cavity-backed circular ring-slot antenna for WBAN applications," *IEEE Antennas Wireless Propag. Lett.*, vol. 15, pp. 1995–1999, 2016.
[13] D. Chaturvedi and S. Raghavan, "Compact QMSIW based antennas for WLAN/WBAN applications," *Prog. Electromagn. Res. C*, vol. 82, pp. 145–153, 2018.
[14] J. Lacik, T. Mikulasek, Z. Raida, and T. Urbanec, "Substrate integrated waveguide monopolar ring-slot antenna," *Microw. Opt. Technol. Lett.*, vol. 56, no. 8, pp. 1865–1869, Aug. 2014.
[15] D. Chaturvedi and S. Raghavan, "Circular quarter-mode SIW antenna for WBAN application," *IETE J. Res.*, vol. 64, no. 4, pp. 482–488, 2018.
[16] G. Muntoni, G. A. Casula, G. Montisci, T. Pisanu, H. Rogier, and A. Michel, "An eighth-mode SIW antenna for low-power wide-area network applications," *J. Electromagn. Waves Appl.*, vol. 35, no. 13, pp. 1815–1829, Sep. 2021.
[17] X. Zhu, X. Liu, and H. Yang, "Compact dual-band wearable textile antenna based on quarter-mode substrate integrated waveguide," in *Proc. 9th Asia–Pacific Conf. Antennas Propag. (APCAP)*, Xiamen, China, Aug. 2020, pp. 1–2.

[18] S. Yan, P. J. Soh, and G. A. E. Vandenbosch, "Dual-band textile MIMO antenna based on substrate-integrated waveguide (SIW) technology," *IEEE Trans. Antennas Propag.*, vol. 63, no. 11, pp. 4640–4647, Nov. 2015.
[19] S. Devalal and A. Karthikeyan, "LoRa technology—An overview," in *Proc. 2nd Int. Conf. Electron., Commun. Aerosp. Technol. (ICECA)*, Coimbatore, India, Mar. 2018, pp. 284–290.
[20] (May 2015). *Semtech AN 120022 LoRa Modulation Basics*. [Online]. Available: https://www.frugalprototype.com/wpontent/uploads/2016/08/an1200.22.pdf
[21] B. Oniga, V. Dadarlat, E. De Poorter, and A. Munteanu, "Analysis, design and implementation of secure LoRaWAN sensor networks," in *Proc. 13th IEEE Int. Conf. Intell. Comput. Commun. Process. (ICCP)*, Cluj-Napoca, Romania, Sep. 2017, pp. 421–428.
[22] A. Iqbal, M. Al-Hasan, I. B. Mabrouk, and M. Nedil, "Compact SIW-based self-quadruplexing antenna for wearable transceivers," *IEEE Antennas Wireless Propag. Lett.*, vol. 20, no. 1, pp. 118–122, Jan. 2021.
[23] B. Mandal and S. K. Parui, "Wearable tri-band SIW based antenna on leather substrate," *Electron. Lett.*, vol. 51, no. 20, pp. 1563–1564, Oct. 2015.
[24] R. Cicchetti, V. Cicchetti, A. Faraone, L. Foged, and O. Testa, "A compact high-gain wideband lens Vivaldi antenna for wireless communications and through-the-wall imaging," *IEEE Trans. Antennas Propag.*, vol. 69, no. 6, pp. 3177–3192, Jun. 2021.
[25] K. Lu, K. W. Leung, and N. Yang, "3-D-printed circularly polarized twisted-ridge horn antenna," *IEEE Trans. Antennas Propag.*, vol. 69, no. 3, pp. 1746–1750, Mar. 2021.
[26] K.-P. Lätti, M. Kettunen, J.-P. Ström, and P. Silventoinen, "A review of microstrip T-resonator method in determining the dielectric properties of printed circuit board materials," *IEEE Trans. Instrum. Meas.*, vol. 56, no. 5, pp. 1845–1850, Oct. 2007.
[27] G. Q. Luo, Z. F. Hu, L. X. Dong, and L. L. Sun, "Planar slot antenna backed by substrate integrated waveguide cavity," *IEEE Antennas Wireless Propag. Lett.*, vol. 7, pp. 236–239, 2008.
[28] M. Bozzi, A. Georgiadis, and K. Wu, "Review of substrate-integrated waveguide circuits and antennas," *IET Microw., Antennas Propag.*, vol. 5, no. 8, pp. 909–920, Jun. 2011.
[29] G. A. Casula, A. Michel, G. Montisci, P. Nepa, and G. Valente, "Energy-based considerations for ungrounded wearable UHF antenna design," *IEEE Sensors J.*, vol. 17, no. 3, pp. 687–694, Feb. 2017.
[30] *IEEE Standard for Safety Levels With Respect to Human Exposure to Radio Frequency Electromagnetic Fields*, IEEE Standard C95.1, 3 kHz to 300 GHz, 1999.

GIOVANNI ANDREA CASULA (Senior Member, IEEE) received the M.S. degree in electronic engineering and the Ph.D. degree in electronic engineering and computer science from the Università degli Studi di Cagliari, Cagliari, Italy, in 2000 and 2004, respectively.

Since December 2017, he has been an Associate Professor of electromagnetic fields with the Università degli Studi di Cagliari, teaching courses in electromagnetics and antenna engineering. He has authored or coauthored about 50 articles in international journals. His current research interests include analysis and design of waveguide slot arrays, RFID antennas, wearable antennas, and numerical methods in electromagnetics.

GIORGIO MONTISCI (Senior Member, IEEE) received the M.S. degree in electronic engineering and the Ph.D. degree in electronic engineering and computer science from the Università degli Studi di Cagliari, Cagliari, Italy, in 1997 and 2000, respectively. Since February 2022, he has been a Full Professor of electromagnetic fields with the Università degli Studi di Cagliari, teaching courses in electromagnetics and microwave engineering. He has authored or coauthored about 80 articles in international journals. His current research interests include analysis and design of waveguide slot arrays, RFID antennas, wearable antennas, numerical methods in electromagnetics, and microwave circuits and systems. He was awarded the IEEE Access Outstanding Associate Editor of 2020 and 2021. He is an Associate Editor of IEEE Access, *IET Microwaves, Antennas and Propagation*, and *IET Electronics Letters*, and an Academic Editor of the *International Journal of Antennas and Propagation*.

GIACOMO MUNTONI received the bachelor's degree in electronic engineering, the master's degree in telecommunication engineering, and the Ph.D. degree in electronic engineering and computer science from the Università degli Studi di Cagliari, Cagliari, Italy, in 2010, 2015, and 2019, respectively.

He is currently working as a Technologist with the Applied Electromagnetics Group, Università degli Studi di Cagliari. His research interests include design and characterization of antennas for biomedical and aerospace applications, wearable antennas, microwave–based dielectric characterization of materials, 3D-printed antennas, and space debris monitoring in low earth orbit.

Open Access funding provided by 'Università degli Studi di Cagliari' within the CRUI CARE Agreement